Catalysis Science & Technology

Accepted Manuscript

ROYAL SOCIETY OF CHEMISTRY

www.rsc.org/catalysis

Catalysis Science & Technology RSCPublishing

ARTICLE

Ethylene Formation by Methane Dehydrogenation and C-C Coupling Reaction on Stoichiometric IrO_2 (110) Surface -A Density Functional Theory Investigation†

Cite this: DOI: 10.1039/xoxxoooooox

Received ooth January 2012,
Accepted ooth January 2012

DOI: 10.1039/xoxxoooooox

www.rsc.org/

T. L.M. Pham, E.G. Leggesse and J.C.Jiang*

The capability to activate methane at mild temperature and facilitate all elementary reactions on the catalyst surface is a defining characteristic of an efficient catalyst especially for the direct conversion of methane to ethylene. In this work, theoretical calculations are performed to explore such catalytic characteristic of IrO_2 (110) surface. The energetics and mechanism for methane dehydrogenation reactions, as well as C-C coupling reactions on the IrO_2 (110) surface, are investigated by using van der Waals-corrected Density Functional Theory calculations. The results indicate that, non-local interaction significantly increases the binding energy of CH_4 molecule with IrO_2 (110) surface by 0.35 eV. Such interaction facilitates molecular-mediated mechanism for the first C–H bond cleavage with a low kinetic barrier of 0.3 eV which is likely to occur at mild temperature condition. Among the dehydrogenation reactions of methane, CH_2 dissociation into CH has highest activation energy of 1.19 eV, making CH_2 the most significant monomeric building block on IrO_2 (110) surface. Based on the DFT calculations, the formation of ethylene could be feasible on IrO_2 (110) surface via selective CH_4 dehydrogenation reactions to CH_2 and barrierless self-coupling reaction of CH_2 species. The results provide an initial basis for understanding and designing efficient catalyst for the direct conversion of methane to ethylene under mild temperature.

Introduction

The abundance of natural gas resource along with the advancement of shale gas extraction technology makes methane a valuable raw material for the petrochemical industry. Conversion of methane to hydrocarbons can be achieved through an indirect or a direct route.[1] The indirect route involves the multi-step method of producing higher hydrocarbons via intermediates (syngas) formed from the reforming processes. Whereas the direct conversion involves oxidative coupling of methane in the presence of oxidant or non-oxidative coupling via homologation of methane in the absence of oxidant. The current industrial scale production of higher hydrocarbons from methane involves indirect conversion via synthesis gas production [2, 3] followed by Fischer-Tropsch synthesis.[4] Even though the need for high activation energy and selectivity remain to be a challenge, direct conversion of methane eliminates the cost of producing synthesis gas thereby significantly improving methane utilization. Therefore, enormous effort has been devoted to develop a cost-effective method to convert methane directly into value-added chemicals[5-8], and selective oxidation of methane is arguably the most promising route. The selective oxidation of methane to C_2 hydrocarbons[9-11], particularly to ethylene, is of great interest since ethylene is an important feedstock for the vast range of industrial chemical synthesis. Although the selective conversion of methane to C_2 hydrocarbons would lead to tremendous economic benefits, efficient catalysts with high CH_4 conversion and C_2 hydrocarbons selectivity have not yet been achieved which prevents this process from large-scale production.

So far, numerous catalysts[12-14] have been synthesized and extensively studied for the selective oxidation of methane to ethylene with several types of oxidants such as, O_2, H_2O_2, and CO_2. Among them, Li-doped MgO[10, 15-18] and La_2O_3-based[19-25] catalysts have been most studied for oxidative coupling of methane (OCM) using O_2 as an oxidant. Because of the chemical inertness of CH_4 molecule, these catalysts generally require high operating temperatures (ca. 800^0C) for the initial C-H bond breaking to generate free methyl radical on the catalyst surface. Under such high temperature, methyl radical once formed desorb easily to the gas-phase leading to the coupling reactions to form C_2 hydrocarbon products.[26-30] However, with the presence of O_2 in the gas phase, high temperature condition tends to promote over-oxidation process, triggering secondary gas-phase reactions with O_2 generating CO_x products that suppress the C_2 hydrocarbon selectivity and enhance greenhouse gas emission. Despite recent effort to

mitigate over-oxidation reaction by employing sulfur as "soft" oxidant[31] or by considering non-oxidative conversion of methane[32], the methane conversion process was required to operate at very high reaction temperature, raising heat management and reactor design issues. Accordingly, an effective catalyst for selective methane conversion to ethylene should not only be able to activate CH_4 at mild temperature but also facilitate the selective dehydrogenation and C-C coupling reactions on its surface.[33] Based on these criteria, it is possible to screen theoretically whether the candidate catalyst satisfies these criteria before conducting experimental work.

Species	Eb (eV)	d(C-H)(Å)	d(Ir_{cus}-C) (Å)
CH_4	0.76 (0.41)	1.15[a],1.09	2.51
CH_3	2.99 (2.68)	1.10	2.07
CH_2	4.54 (4.13)	1.10	1.87
CH	4.69 (4.62)	1.09	1.75
C	5.43 (5.34)	-	1.72

Table 1 Binding energies, C-H bond lengths and Ir_{cus}-C bond distances of CH_x (x = 0-4) on IrO_2(110). Binding energies in parenthesis are calculated with PBE functional.

[a]Length of C-H bond undergoing interaction with Ir_{cus}

Understanding the chemistry of methane on metal and metal oxide surfaces is a stepping stone towards designing efficient catalyst for methane transformation processes, including OCM, selective oxidation of methane, methane combustion, and solid-oxide fuel cell application. Dissociative chemisorption of methane on well-defined surface can occur following two distinct mechanisms: a direct dissociative mechanism and a trapping-mediated mechanism. On noble transition metal surface, highly coordinatively unsaturated (cus) sites play role in lowering the activation barrier for methane dissociation. For instance, facile dissociation of methane on Ir (111)[34] and Ir (110)[35] single crystal surfaces were investigated by molecular beam and bulb gas techniques, showing that trapping-mediated mechanism is dominating mechanism at low gas temperature. The trapping-mediated mechanism was also reported in the case of alkane dissociation on PdO (101) surface at low-temperature.[36-38] On the PdO (101) surface, alkane molecule is activatedly adsorbed by forming dative bonds with Pd_{cus} atoms, and followed by the initial C-H bond cleavage. Likewise, Ir_{cus} on IrO_2(110) surface are also expected to act in similar manner as Pd_{cus} in activating methane. [39, 40]

By using density function theory calculations, Wang and co-workers[41] reported that CH_4 is significantly activated when molecularly adsorbs on IrO_2(110) surface through agostic interaction between the C-H bonding orbital and the d_z^2 orbital of surface Ir_{cus} atom. This unique σ-d interaction weakens Ir-coordinated C-H bonds, making the barrier for C-H bond cleavage notably lower than CH_4 desorption energy, suggesting that trapping-mediated mechanism is the preference of CH_4 dissociation at mild temperature on IrO_2(110) surface. This result motivates us to go further and explore the methane activation, dehydrogenation and the possibility of the coupling reactions to C_2 hydrocarbons on IrO_2 (110) surface.

In this work, we carried out van der Waals inclusive density functional theory calculations to investigate the thermodynamics and kinetics of successive C-H bond breakings in methane to form methyl (CH_3), methylene (CH_2), methylidyne (CH) and carbon atom (C) on IrO_2(110) surface. The coupling reactions of stabilized CH_x species on IrO_2 (110) surface are also investigated. Moreover, the adsorption of CH_x (x=1-3) on IrO_2 (110) surface were characterized by analyzing the density of states (DOS) and electron density difference (EDD) contours.

Computational Details

All periodic DFT calculations in this study were performed with the generalized gradient approximation (GGA) of Perdew-Burke-Ernzerhof (PBE) exchange-correlation functional[42] employing Vienna ab initio simulation program (VASP 5.2.12).[43, 44] The projector augmented wave (PAW) method[45] was applied to describe the electron core interactions. The Kohn–Sham orbitals are expanded in a plane-wave basis set with kinetic energy cutoff of 450 eV. To study the effect of van der Waals interaction on thermodynamics and kinetic of the reactions, calculations were also performed with optB88-vdW functional[4647], which was chosen based on the result from benchmark calculations as showed in Table S1 in Supporting information. The convergence threshold was set to be 10^{-5} eV for the total electronic energy in the self-consistent loop. The atomic positions were relaxed using either quasi-Newton algorithm or damped molecular dynamics scheme until the x, y, z-components of unconstrained atomic force were smaller than $2x10^{-2}$ eV/Å.

The IrO_2(110) surface was modeled by twelve-layer slab with the lowest six layers being kept fixed. In all case, a p(3x1) lateral supercell was used containing a vacuum space of 15 Å between the slab and its periodic replicas. The [001], [$\bar{1}$10]and [110] crystallographic directions of the slab were defined as the *x*, *y*, and *z* Cartesian coordinates of the supercell. The stoichiometric IrO_2(110) surface exhibits fivefold coordinated Ir (Ir_{cus}) atoms and twofold coordinated oxygen atoms occupying the bridge sites (O_{br}) as the active sites for adsorption and surface reaction processes. The Brillouin zone was sampled with a 4 x 6 x 1 Monkhorst-Pack mesh.[48] The Climbing Image Nudged Elastic Band (CI-NEB) method[49] with eight images was applied for finding transition states and minimum energy path of all reactions. The normal-mode frequency analysis was performed for validating the optimized and transition state structures. Since zero-point energy (ZPE) is known to play a significant role in dehydrogenation reactions, [50, 51] all the reaction energetics reported in this work was corrected accordingly.

The binding energy (E_b) of CH_x with the surfaces is defined by the formula: $E_b = (E_{CH_x} + E_{Surf}) - E_{CH_x/Surf}$, where E_{surf} is the total energy of the clean IrO_2(110) surface, E_{CHx} is the total energy of free CH_x fragment, and $E_{CHx/Surf}$ is the total energy of the surface together with the adsorbate. For the reference energy of isolated CH_x fragment, calculations were done by putting them in a cubic cell with 15 Å side lengths. The electron density difference (EDD) is defined as: $\rho_{diff} = \rho_{CH_x/Surf} - (\rho_{CH_x} + \rho_{Surf})$, where $\rho_{CHx/Surf}$ denotes electron density of CH_x adsorbed on IrO_2(110) surface, while ρ_{CHx} and ρ_{Surf} represent the charge densities of isolated CH_x fragment and clean IrO_2(110) surface, respectively. EDD contour plots were created by using VESTA program.[52]

Results and Discussion

Adsorption of CH_x (x= 0–4) on IrO_2(110) surface

To understand the interactions of different species with the surface, we first investigated adsorption of CH_x (x= 0–4) species on IrO_2(110) surface. The calculated binding energies and Ir_{cus}–C bond lengths are summarized in Table 1. As can be seen from the Table, the binding energies of CH_x increase and the Ir_{cus}–C bond lengths decrease with a decrease in the number of their H atoms. These trends are attributed to the fact that the less number of H atoms in CH_x species the more free valence electrons it possesses, which results in the stronger interactions between CH_x with IrO_2(110) surface and the shorter Ir_{cus}–C bond lengths. However, the C-H bond lengths in most of the cases are about 1.10 Å indicating the geometry of adsorbed CH_x do not change significantly upon adsorption. It should be noted that, the order of binding energy of CH_x with IrO_2(110) surface are similar to those of NH_x on RuO_2(110) and IrO_2(110) surface.[53, 54]

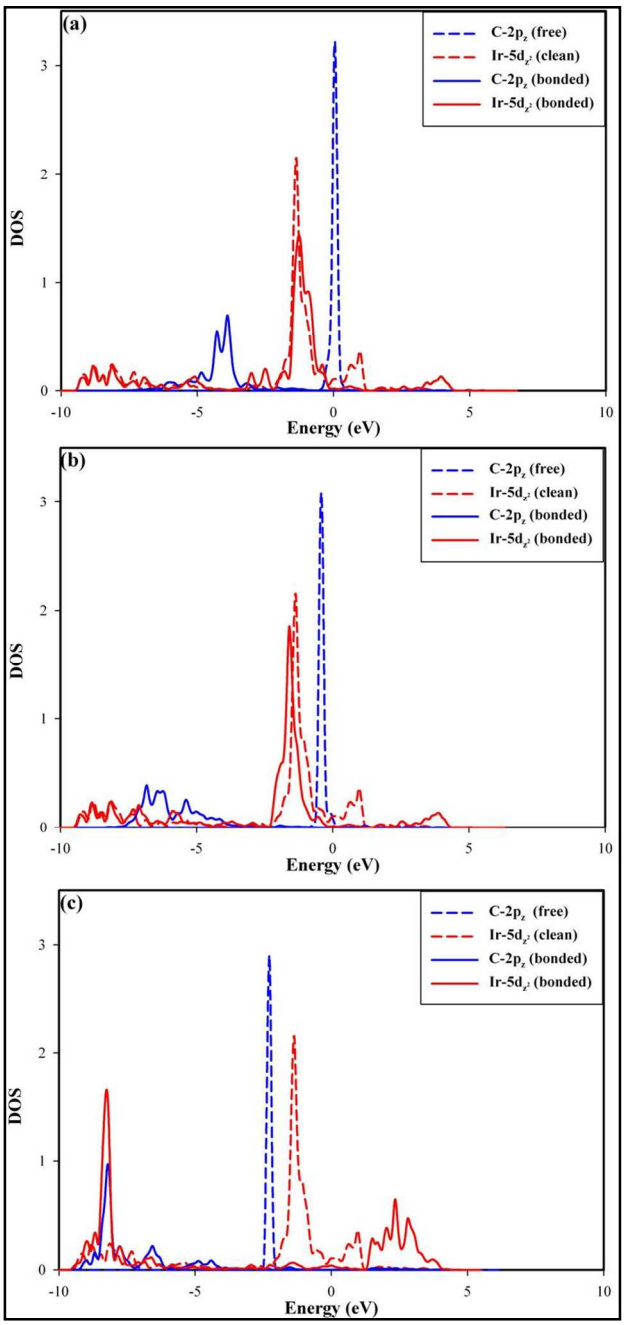

Fig.1 (Colour online) PDOS plot of σ interactions between the C-2p_z of CH_x and Ir_{cus} -5d_{z2} in the adsorption models: a) CH_3; b) CH_2; c) CH. The blue and red lines correspond to C-2p_z and Ir_{cus} -5d_z^2; the dashed and solid lines correspond to before and after adsorption.

The conventional DFT calculation with PBE functional gives the CH_4 binding energy of 0.41 eV, which is similar to the value reported by PW91 functional.[41] When considering DFT with van der Waals correction, the binding energy increases to 0.76 eV, which is 0.10 eV higher than the estimated value reported by Weaver.[55] Non-local interaction of 0.35 eV is indeed important when studying the interaction between CH_4 and IrO_2(110) surface. However, local interaction through special σ-d interaction[41] is noteworthy stronger than non-local interaction, which is in contrast with the case on PdO(101) surface.[56] Thus, it can be suggested that local interaction makes more contribution to the CH_4 binding energy than non-local

interaction. For this reason, calculation with optB88-vdW functional results in the same Ir_{cus}–C bond length with that of PBE. In comparison with other surfaces, both local and non-local interaction of CH_4 with $IrO_2(110)$ surface are significantly higher than those with Pd(111) and PdO(101).[57]
CH_4 is molecularly adsorbed on the top site of the surface with the least adsorption energy among CH_x (x= 0–4) species. This stems from the fact that the atoms in CH_4 are saturated in their coordination with the C−H bond exhibiting a low polarity. Similarly, CH_x (x= 0–3) species also prefer to adsorb on the top of Ir_{cus} atom. Because of unsaturated nature, CH_x (x= 0–3) species chemically bond to the surface with much higher binding energy than CH_4. CH_x (x= 0–3) species only interact with Ir_{cus} through carbon atom. The differences between binding energies by PBE and optB88-vdW are relatively small compared to their absolute values. In contrast with the case of CH_4 adsorption, non-local interaction makes slighter contribution to the binding energy of the radical species. Thus, non-local interaction plays more important role in closed-shell molecular adsorption than open-shell species adsorption, which is in line with the recent study.[58]

Methyl radical is found to adsorb on top of iridium atom with the Ir_{cus}-C bond distance of 2.07Å. Identical H-C-H angles (109.6^0) in the non-planar adsorbed CH_3 molecule indicate that the carbon atom adopts sp^3 hybridization which is different from the sp^2 hybridized carbon in the gas phase planar CH_3 radical. CH_3 bound to surface through σ interaction between the nonbonding molecular orbital (singly occupied molecular orbital, n-CH_3) with Ir_{cus} -$5d_{z^2}$ orbital since n-CH_3 orbital points towards Ir_{cus} atom and their energy levels are relatively close. The σ interaction between n-CH_3 orbital and Ir_{cus} -$5d_{z^2}$ orbital in principle occurs due to the overlap between C-$2p_z$ and Ir_{cus} -$5d_{z^2}$ orbitals. The PDOS analysis in Figure 1a reveals the existence of strong σ interaction between CH_3 species and IrO_2 (110) surface. The blue and red lines correspond to the DOS of C-$2p_z$ in CH_3 species and Ir_{cus} -$5d_{z^2}$ of IrO_2 (110) surface, respectively. In the case of adsorbed CH_3, both C-$2p_z$ and Ir_{cus} -$5d_{z^2}$ bands become delocalized, clearly indicating strong σ interaction between CH_3 and surface. The σ interaction pushes the Ir_{cus} -$5d_{z^2}$ up above the Fermi level, resulting in a decrease in Ir_{cus} -$5d_{z^2}$ electron density. Since the n-CH_3 orbital is initially singly occupied, upon the σ interaction, electron will transfer from Ir_{cus} -$5d_{z^2}$ orbital to Ir_{cus}-CH_3 bonding orbital. As a result, the bonding of CH_3 on the surface mostly exhibits ionic character. The increase in electron density around C atom, as depicted in the electron density difference (EDD) contour plots in Figure 2a and 2b, also demonstrates the ionic character of Ir_{cus}-CH_3.

In comparison to the methyl, the CH_2 fragment has stronger interaction with surface which causes the shorter Ir_{cus}-C bond distance (1.87 Å). The H-C-H and H-C-Ir_{cus} bond angles are 115.3^0 and 122.3^0, respectively, indicative of sp^2 hybridization. For CH_2 species, in addition to σ interaction between $2a_1$ orbital and Ir_{cus} -$5d_{z^2}$ orbital (Figure 2c), there also exists another π interaction between C-$2p_y$ orbital and Ir_{cus}-$5d_{yz}$ orbital which is clearly seen in the EDD plot in the Figure 2d. Similar to CH_3, σ interaction between $2a_1$ CH_2 orbital and Ir_{cus} -$5d_{z^2}$ orbital also occur mainly through the overlap of C-$2p_z$ and Ir_{cus} -$5d_{z^2}$ orbitals. However, compared to the case of CH_3, both C-$2p_z$ and Ir_{cus} -$5d_{z^2}$ shows a further shift to -6 eV while the location of anti-bonding orbitals in both cases remains essentially the same. This evidence reveals that CH_2 has stronger σ interaction with surface than CH_3 due to the lower energy level C-$2p_z$ orbital in the free CH_2 fragment. In general, π interaction between C-$2p_y$ and Ir_{cus}-$5d_{yz}$ orbitals is relatively weak in comparison with σ interaction between C-$2p_z$ orbital and Ir_{cus} -$5d_{z^2}$ orbital.[59] Therefore, stronger σ interaction is the primary reason that CH_2 has higher binding energy with $IrO_2(110)$ surface than CH_3.

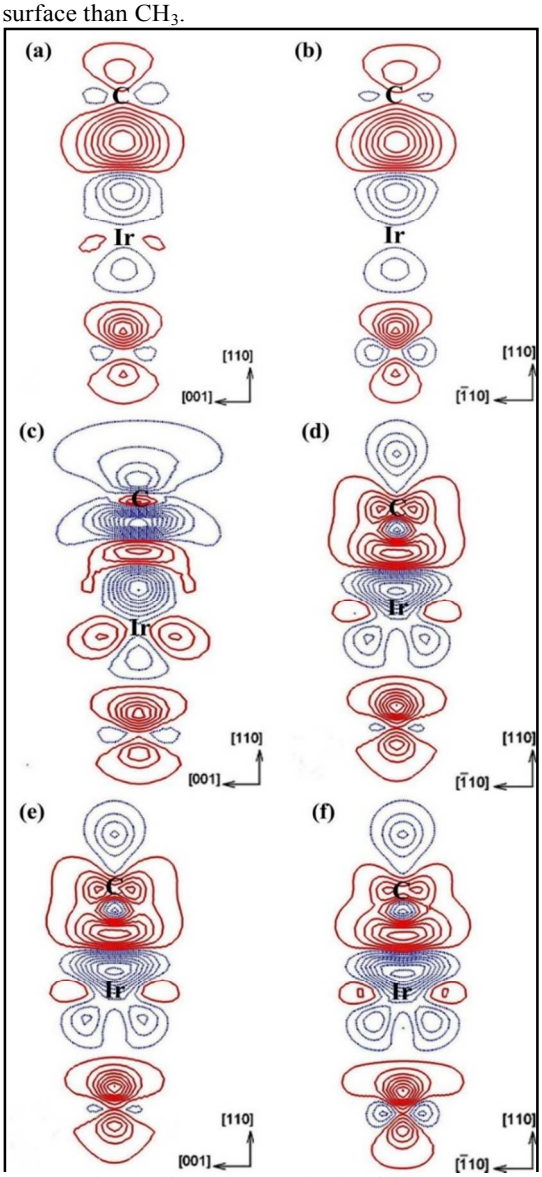

Fig.2 (Colour online) Electron density difference contour plots of CH_x (x=1-3) on $IrO_2(110)$ surface: (a, b) CH_3 ; (c, d) CH_2 ; (e, f) CH. The solid red and dashed blue lines represent increasing and decreasing electron densities, respectively.

CH is adsorbed perpendicular to the $IrO_2(110)$ surface, with the Ir_{cus}-C bond distance of 1.75 Å. Carbon atom in the adsorbed CH adopts sp hybridization which allows C-$2p_x$ and C-$2p_y$ orbitals to be parallel to $IrO_2(110)$ surface. As shown in the EDD contour plot in Figure 2e and 2f, such orientation of the orbitals results in possible π interactions with Ir_{cus}-$5d_{xz}$ and Ir_{cus}-$5d_{yz}$ orbitals. Similar to CH_2, σ interaction between CH and surface also occurs mainly through the overlap between C-$2p_z$ and Ir_{cus} -$5d_{z^2}$ orbitals. The PDOS plot in Figure 1c shows that the location of bonding orbital is around - 8 eV which is lower than in the case of CH_2 fragments. However, the

downshift of C-2p_z peak in both case are the same (about 6 eV). Therefore, the σ interactions of CH_2 and CH with IrO_2(110) surface have similar strength. Consequently, the binding energies of CH_2 and CH with IrO_2(110) surface are comparable. The small binding energy difference comes from an additional weak π interaction between C-2p_x and Ir_{cus}-5d_{xz}.

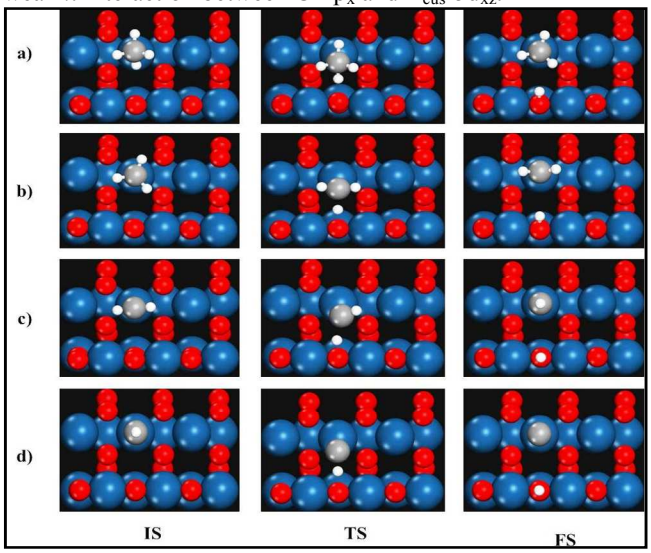

Fig.3 (Colour online) Initial state, transition state and final state for dehydrogenation reaction of: a) CH_4, b) CH_3, c) CH_2, d) CH on IrO_2(110) surface.

CH_x dehydrogenation on IrO_2(110) surface

After molecularly adsorbed on IrO_2(110) surface, CH_4 undergo successive catalytic dissociations to CH_3, CH_2, CH and C surface fragments. To explore the relative stability of CH_x (x=0–3) intermediates, we have performed a series of calculations on dehydrogenation reactions of CH_4 on IrO_2(110) surface. In our calculations, the dehydrogenation processes involve hydrogen atom transferring from CH_x (x=1–4) to O_{br} atom, assuming that the detached H atoms can be removed from the surface and the remaining fragment is considered as the initial state for the next dehydrogenation reaction. The reaction energetics of four successive dehydrogenation reactions are listed in Table 2. The Initial state, transition state and final state optimized geometries for dehydrogenation reactions are also shown in Figure.3.

With relatively high adsorption energy, the initial CH_4 dissociation to CH_3 on IrO_2(110) surface is likely to occur by trapping-mediated mechanism via breaking of the activated C-H bond, especially under low-temperature condition. Our calculations with PBE functional report that the activation energy and reaction energy of this step are 0.25 eV and -1.09 eV respectively. These energetic values are in good agreement with previous values obtained from PW91 functional.[41] However, the activated C-H bond length of the transition state structure

Reaction	E_{act}(eV)	ΔE(eV)	d(C-H)(Å)	IMF (cm^{-1})
$CH_4 \rightarrow CH_3+H$	0.30 (0.25)	-1.09 (-1.09)	1.30	i1127
$CH_3 \rightarrow CH_2+H$	0.63 (0.61)	-0.08 (0.06)	1.34	i1397
$CH_2 \rightarrow CH+H$	1.19 (1.15)	0.98 (0.99)	1.48	i1160
$CH \rightarrow C+H$	0.24 (0.22)	-0.49 (-0.48)	1.20	i739

Table 2 Activation Barriers (E_{act}, eV), Reaction energies (E_{react},eV), Activated C-H bond lengths of transition state and Imaginary frequencies (IMF, cm^{-1}) for Dehydrogenation reactions on IrO_2 (110). The energy values in parenthesis are calculated with PBE functional.

reported by using PBE functional is remarkably shorter than that calculated with PW91 functional (1.3 Å vs 1.4 Å). The van der Waals-corrected DFT calculations report almost the same reaction energetics with conventional DFT, suggesting insignificant role of the non-local interaction in the energetics of CH_4 dissociation. However, when considering both CH_4 adsorption and dissociation steps, , non-local interaction results in depressing the dissociation energy level more below the zero-energy level, as can be seen in Figure 4. These results strengthen the prediction that CH_4 dissociation is more preferable than the desorption on IrO_2(110) surface.[41]These results also support the prediction of Weaver[55] that the dissociation process probably occur at temperature lower than 150 K.

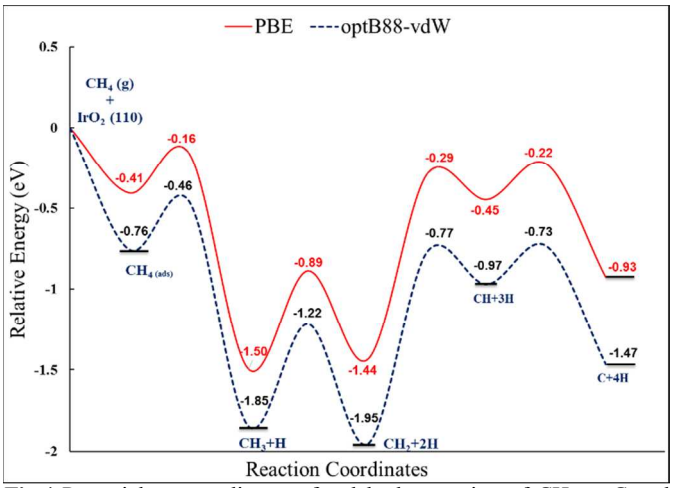

Fig.4 Potential energy diagram for dehydrogenation of CH_4 to C and 4H on IrO_2(110) surface.

Similar to methane, the dehydrogenation of methyl is also relatively easy process with the activation energy of 0.63 eV, and is slightly exothermic (-0.08 eV). Along the reaction coordinate, CH_3 is slightly rotated and shifted toward O_{br} atom. The C-H bond pointing toward O_{br} atom is elongated from 1.10 Å in the initial state to 1.34 Å in the transition state. The third dehydrogenation of CH_2 to CH has highest activation energy (1.19 eV), which is nearly double the second highest barrier (0.63 eV). The kinetically unfavorable nature of the third dehydrogenation reaction stems from its endothermic character (0.98 eV). In this transition state, CH_2 is rotated about 90 degrees before the detached H atom transfers to O_{br}, and the activated C-H bond length is about 1.48 Å. Among the dehydrogenation reactions, the last dehydrogenation reaction is the most facile one with low kinetic barrier of 0.24 eV and a relatively high exothermicity of - 0.49 eV. Along the reaction coordinate, CH is bent toward the O_{br}. In the transition state, the activated C-H bond length is about 1.20 Å which is the shortest among all dehydrogenation reaction transition states.

When comparing all the dehydrogenation reactions, the C-H bond breaking activation energies follow the trend CH < CH_4 < CH_3 < CH_2, which is reverse order with previously reported values on some metal sulfide surfaces.[31] It is noteworthy that the order of C-H bond activation energies follow the same trend

with the activated C-H bond length of the corresponding transition state. Since all dehydrogenation reactions occur on $IrO_2(110)$ surface, entropy losses when changing from initial states to transition states are negligible. As a result, the C-H bond breaking of CH_2 intermediate is the rate-determining step for the dehydrogenation reactions. The highest activation energy of CH_2 among all CH_x dehydrogenation reactions can be explained from the three-dimensional electron density difference of CH_x on $IrO_2(110)$ surface (Figure S2 in Supporting information). The significant electron redistributions to O_{br} atoms in the case of CH_4, CH_3, and CH adsorptions make those atoms become more negatively charged than in the case of CH_2 adsorption. The ability to abstract H from C-H bond of O_{br} is disproportional to the amount of negative charge on it. Therefore, the abstraction of H from CH_2 is the most difficult on $IrO_2(110)$ surface. This observation is strikingly different with the process on almost all transition metal surfaces where the CH dissociation is the rate-determining step.[60-64]

Based on the calculated results, it can be inferred that CH_2 is kinetically significant intermediate and is the most abundant species on $IrO_2(110)$ surface. Therefore, by controlling the reaction condition at mild temperature, it could be possible to block CH_4 dehydrogenation after the first two dehydrogenation reactions and achieve selective dehydrogenation to CH_2. This distinct catalytic activity of $IrO_2(110)$ surface would open a catalytic route to C_2 products by controlling the reaction temperature.

Table 3 Activation Barriers (E_{act}, eV), Reaction energies (E_{react},eV), Activated C-H bond lengths of transition state and Imaginary frequencies (IMF, cm^{-1}) for Dehydrogenation reactions on IrO_2 (110). The energy values in parenthesis are calculated with PBE functional.

Reaction	E_{act}(eV)	E_{react}(eV)	IMF(cm^{-1})
$CH_3+CH_3 \rightarrow C_2H_6$	2.90 (2.89)	0.79 (0.76)	i947
$CH_3+CH_2 \rightarrow C_2H_5$	0.84 (0.85)	-0.64 (-0.72)	i694
$CH_2+CH_2 \rightarrow C_2H4$	0.01 (0.01)	-1.27 (-1.45)	i131

C-C coupling reactions on $IrO_2(110)$ surface

The C_2 product formation depends on the energetics of coupling reactions of adsorbed CH_x species. Thus, the next crucial step is examining the possibility of the C-C coupling reactions on $IrO_2(110)$ surface. By controlling reaction temperature, it is expected that the CH_2 and CH_3 intermediates dominate on $IrO_2(110)$ surface. Therefore, we limit our calculation to the C-C coupling reactions by surface CH_2 and CH_3 intermediates. The initial, transition and final structures of three coupling reactions are showed in Figure 5 while the reaction energetics are summarized in Table 3.

As can be seen from the Figures, the CH_3/CH_3, CH_3/CH_2 and CH_2/CH_2 coupling reactions need to pass through transition states in which the C-C distances are 2.24 Å, 2.19 Å and 2.73 Å respectively. The calculated C-C distance in the transition state of the CH_2/CH_2 coupling reaction is much longer than what is observed in the transition states of the remaining coupling reactions. Thus it can be concluded that, unlike the CH_3/CH_3 and CH_3/CH_2 coupling reactions, CH_2/CH_2 coupling reaction prefers to pass through a very early transition state. In the three coupling reactions the transition states only possess one imaginary frequency involving the C-C bond stretching, which are -947 cm^{-1}, -694 cm^{-1} and -131 cm^{-1} for CH_3/CH_3, CH_3/CH_2 and CH_2/CH_2 respectively. As can be seen from Table 3, self-coupling reaction of CH_3 is the most difficult among the coupling reactions. High activation energy (2.90 eV) combined with unfavorable thermodynamics indicates that the coupling reaction of CH_3/CH_3 radicals to form C_2H_6 is unlikely to occur on $IrO_2(110)$ surface, which is similar with on some metal sulfide surfaces.[31] The coupling reaction of CH_3/CH_2 fragments is an exothermic process of -0.64 eV. However, kinetic barrier of this reaction (0.84 eV) is higher than for CH_3 dehydrogenation reaction (0.63 eV). Therefore, the coupling of CH_3/CH_2 and CH_3 dehydrogenation are competitive reactions. Of all the considered coupling reactions, the self-coupling reaction of CH_2 is extremely favorable which is almost barrierless and highly exothermic of -1.27 eV. The lowest barrier of the CH_2/CH_2 coupling reaction is largely due to the reaction passing through a very early transition state. In addition, it is also due to the self-coupling of CH_2 which is less impeded by the repulsion of surrounding H atoms than the other couplings.

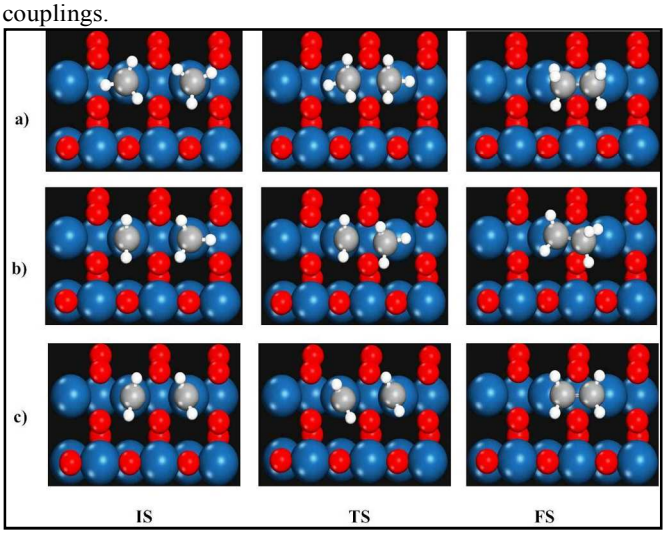

Fig.5 Structure of initial states, transition states and final states for C-C coupling reactions on $IrO_2(110)$. Structure of initial states, transition states and final states for C-C coupling reactions on $IrO_2(110)$.

Based on the results, it can be inferred that none of the CH_3/CH_3, CH_3/CH_2 coupling reactions and CH_2 dehydrogenation can compete with the CH_2/CH_2 coupling reaction. Moreover, the self-coupling of CH_2 to C_2H_4 will take place once CH_2 is generated on the $IrO_2(110)$ surface. The thermodynamics of direct methane conversion to ethylene, including selective CH_4 dehydrogenation reaction to CH_2, coupling of CH_2/CH_2 reaction and desorption energy of ethylene, are depicted in Figure S2 in Supporting information. The high energy released from CH_4 adsorption, dehydrogenation, and CH_2/CH_2 coupling reactions would further facilitate ethylene desorption from $IrO_2(110)$ surface.

Conclusions

We have performed van der Waals-corrected DFT Calculations to assess the catalytic property of IrO_2 (100) surface towards methane dehydrogenation and possible formation of ethylene. The catalytic system discussed in this work delivers an efficient and highly productive strategy for ethylene formation at mild temperature. Based on our results, methylene was found to be

kinetically significant intermediate and is the most abundant species on $IrO_2(110)$ surface. Selective dehydrogenation of methylene can be achieved by controlling the reaction temperature, which could hinder the methane dehydrogenation after the first two steps. The results also demonstrated that non-local interaction facilitate the adsorption and initial dissociation of methane on $IrO_2(110)$ surface. The mild reaction temperature for the dissociation of methane combining with facile ethylene formation suggest that $IrO_2(110)$ surface has great potential to be used as a catalyst material for the direct conversion of methane to ethylene at mild reaction temperature.

Acknowledgements

We thank the Ministry of Science and Technology (NSC-101-2113-M-011-004-MY3) for supporting this research financially. We are also grateful to the National Center of High-Performance Computing for donating computer time and facilities.

Notes and references

Department of Chemical Engineering, National Taiwan University of Science and Technology, 43, Keelung Road, Section 4, Taipei 106, Taiwan. E-mail: jcjiang@mail.ntust.edu.tw, Phone: +886-2-27376653, Fax: +886-227376644.

† . Electronic Supplementary Information (ESI) available: The energy profiles for CH_4 conversion to C_2H_4 on $IrO_2(110)$ are shown in the supplementary material. See DOI: 10.1039/b000000x/

1. P. Tang, Q. Zhu, Z. Wu and D. Ma, *Energy & Environmental Science*, 2014, **7**, 2580-2591.
2. R. Horn, K. A. Williams, N. J. Degenstein and L. D. Schmidt, *J. Catal.*, 2006, **242**, 92-102.
3. A. P. E. York, T. c. Xiao, M. L. H. Green and J. B. Claridge, *Catal. Rev. - Sci. Eng.*, 2007, **49**, 511-560.
4. M. E. Dry, *Appl. Catal., A*, 1996, **138**, 319-344.
5. J. H. Lunsford, *Catal. Today*, 2000, **63**, 165-174.
6. A. Holmen, *Catal. Today*, 2009, **142**, 2-8.
7. M. C. Alvarez-Galvan, N. Mota, M. Ojeda, S. Rojas, R. M. Navarro and J. L. G. Fierro, *Catal. Today*, 2011, **171**, 15-23.
8. C. Hammond, S. Conrad and I. Hermans, *ChemSusChem*, 2012, **5**, 1668-1686.
9. G. E. Keller and M. M. Bhasin, *J. Catal.*, 1982, **73**, 9-19.
10. T. Ito and J. H. Lunsford, *Nature*, 1985, **314**, 721-722.
11. J. A. Sofranko, J. J. Leonard and C. A. Jones, *J. Catal.*, 1987, **103**, 302-310.
12. G. J. Hutchings, M. S. Scurrell and J. R. Woodhouse, *Chem. Soc. Rev.*, 1989, **18**, 251-283.
13. U. Zavyalova, M. Holena, R. Schlögl and M. Baerns, *ChemCatChem*, 2011, **3**, 1935-1947.
14. O. V. Krylov, *Catal. Today*, 1993, **18**, 209-302.
15. S. Arndt, G. Laugel, S. Levchenko, R. Horn, M. Baerns, M. Scheffler, R. Schlögl and R. Schomäcker, *Catal. Rev. - Sci. Eng.*, 2011, **53**, 424-514.
16. M. C. Wu, C. M. Truong, K. Coulter and D. W. Goodman, *J. Catal.*, 1993, **140**, 344-352.
17. K. P. Peil, J. G. Goodwin Jr and G. Marcelin, *J. Catal.*, 1991, **131**, 143-155.
18. K. Kwapien, J. Paier, J. Sauer, M. Geske, U. Zavyalova, R. Horn, P. Schwach, A. Trunschke and R. Schlögl, *Angewandte Chemie International Edition*, 2014, **53**, 8774-8778.
19. J. M. Deboy and R. F. Hicks, *J. Catal.*, 1988, **113**, 517-524.
20. K. D. Campbell, H. Zhang and J. H. Lunsford, *J. Phys. Chem.*, 1988, **92**, 750-753.
21. M. S. Palmer, M. Neurock and M. M. Olken, *J. Am. Chem. Soc.*, 2002, **124**, 8452-8461.
22. B. Li and H. Metiu, *J. Phys. Chem. C*, 2011, **115**, 18239-18246.
23. S. Lacombe, C. Geantet and C. Mirodatos, *J. Catal.*, 1995, **151**, 439-452.
24. Y. Lei, C. Chu, S. Li and Y. Sun, *J. Phys. Chem. C*, 2014, **118**, 7932-7945.
25. C. Chu, Y. Zhao, S. Li and Y. Sun, *J. Phys. Chem. C*, 2014, **118**, 27954-27960.
26. D. J. Driscoll and J. H. Lunsford, *J. Phys. Chem.*, 1985, **89**, 4415-4418.
27. D. J. Driscoll, W. Martir, J. X. Wang and J. H. Lunsford, *J. Am. Chem. Soc.*, 1985, **107**, 58-63.
28. K. D. Campbell, E. Morales and J. H. Lunsford, *J. Am. Chem. Soc.*, 1987, **109**, 7900-7901.
29. L. Luo, X. Tang, W. Wang, Y. Wang, S. Sun, F. Qi and W. Huang, *Sci. Rep.*, 2013, **3**.
30. J. H. Lunsford, *Angew. Chem., Int. Ed.*, 1995, **34**, 970-980.
31. Q. Zhu, S. L. Wegener, C. Xie, O. Uche, M. Neurock and T. J. Marks, *Nat Chem*, 2013, **5**, 104-109.
32. X. Guo, G. Fang, G. Li, H. Ma, H. Fan, L. Yu, C. Ma, X. Wu, D. Deng, M. Wei, D. Tan, R. Si, S. Zhang, J. Li, L. Sun, Z. Tang, X. Pan and X. Bao, *Science*, 2014, **344**, 616-619.
33. E. E. Wolf, *Journal of Physical Chemistry Letters*, 2014, **5**, 986-988.
34. D. C. Seets, C. T. Reeves, B. A. Ferguson, M. C. Wheeler and C. B. Mullins, *J. Chem. Phys.*, 1997, **107**, 10229-10241.
35. D. C. Seets, M. C. Wheeler and C. B. Mullins, *Chem. Phys. Lett.*, 1997, **266**, 431-436.
36. J. F. Weaver, S. P. Devarajan and C. Hakanoglu, *J. Phys. Chem. C*, 2009, **113**, 9773-9782.
37. J. F. Weaver, J. A. Hinojosa Jr, C. Hakanoglu, A. Antony, J. M. Hawkins and A. Asthagiri, *Catal. Today*, 2011, **160**, 213-227.
38. J. F. Weaver, C. Hakanoglu, J. M. Hawkins and A. Asthagiri, *J. Chem. Phys.*, 2010, **132**, -.
39. W.-H. Chung, C.-C. Wang, D.-S. Tsai, J.-C. Jiang, Y.-C. Cheng, L.-J. Fan, Y.-W. Yang and Y.-S. Huang, *Surf. Sci.*, 2010, **604**, 118-124.
40. Y. B. He, A. Stierle, W. X. Li, A. Farkas, N. Kasper and H. Over, *J. Phys. Chem. C*, 2008, **112**, 11946-11953.
41. C.-C. Wang, S. S. Siao and J.-C. Jiang, *J. Phys. Chem. C*, 2012, **116**, 6367-6370.
42. J. P. Perdew, K. Burke and M. Ernzerhof, *Phys. Rev. Lett.*, 1996, **77**, 3865-3868.
43. G. Kresse and J. Hafner, *Physical Review B*, 1994, **49**, 14251-14269.
44. G. Kresse and J. Furthmuller, *Computational Materials Science*, 1996, **6**, 15-50.
45. G. Kresse and D. Joubert, *Physical Review B*, 1999, **59**, 1758-1775.
46. J. Klimeš, D. R. Bowler and A. Michaelides, *Physical Review B*, 2011, **83**, 195131.

47. J. Klimeš, D. R. Bowler and A. Michaelides, *J. Phys.: Condens. Matter*, 2010, **22**, 022201.
48. H. J. Monkhorst and J. D. Pack, *Physical Review B*, 1976, **13**, 5188-5192.
49. G. Henkelman, B. P. Uberuaga and H. Jónsson, *J. Chem. Phys.*, 2000, **113**, 9901-9904.
50. D. Sholl and J. A. Steckel, *Density Functional Theory: A Practical Introduction*, John Wiley & Sons, Hoboken, NJ, 2011.
51. A. Groß, in *Theoretical Surface Science*, Springer Berlin Heidelberg, 2009, DOI: 10.1007/978-3-540-68969-0_5, ch. 5, pp. 101-163.
52. K. Momma and F. Izumi, *J. Appl. Crystallogr.*, 2011, **44**, 1272-1276.
53. C.-C. Wang, S. S. Siao and J.-C. Jiang, *J. Phys. Chem. C*, 2010, **114**, 18588-18593.
54. C.-C. Wang, Y.-J. Yang and J.-C. Jiang, *J. Phys. Chem. C*, 2009, **113**, 2816-2821.
55. J. F. Weaver, *Chemical Reviews*, 2013, **113**, 4164-4215.
56. A. Antony, A. Asthagiri and J. F. Weaver, *J. Chem. Phys.*, 2013, **139**, -.
57. A. Antony, C. Hakanoglu, A. Asthagiri and J. F. Weaver, *J. Chem. Phys.*, 2012, **136**, -.
58. J. Ye, C. Liu and Q. Ge, *Phys. Chem. Chem. Phys.*, 2012, **14**, 16660-16667.
59. C. Zheng, Y. Apeloig and R. Hoffmann, *J. Am. Chem. Soc.*, 1988, **110**, 749-774.
60. B. Xing, X.-Y. Pang and G.-C. Wang, *J. Catal.*, 2011, **282**, 74-82.
61. P. W. van Grootel, R. A. van Santen and E. J. M. Hensen, *J. Phys. Chem. C*, 2011, **115**, 13027-13034.
62. B. S. Bunnik and G. J. Kramer, *J. Catal.*, 2006, **242**, 309-318.
63. J. E. Mueller, A. C. T. van Duin and W. A. Goddard, *J. Phys. Chem. C*, 2009, **113**, 20290-20306.
64. S. Yuan, L. Meng and J. Wang, *J. Phys. Chem. C*, 2013, **117**, 14796-14803.

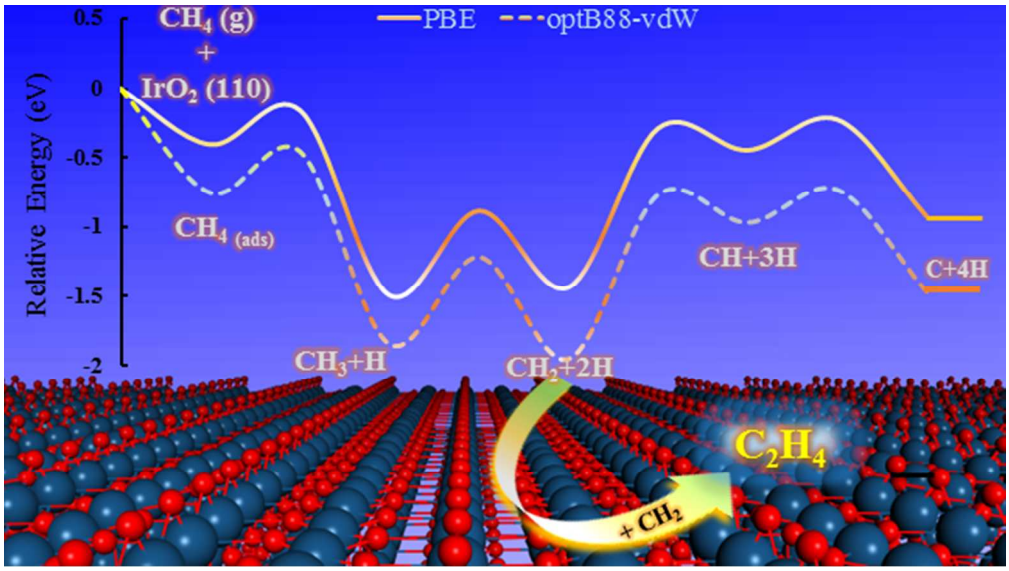

170x95mm (96 x 96 DPI)